Sensorless Control of Dual Three-Phase IPMSM Based on Frequency Adaptive Linear Extended State Observer

Yonggang Li, Yashan Hu, Xiandong Ma, and Li Liu

Abstract—The sensorless control of internal permanent magnet synchronous motor (IPMSM) based on the conventional linear extended state observer (LESO) does not have sufficient capability to eliminate the steady-state position estimation error. To solve this issue, a frequency adaptive LESO (FA-LESO) is proposed to estimate the back electromotive force (BEMF) accurately. The gains of the proposed observer are designed according to the pre-designed transfer function of a second-order complex-coefficient filter, whose stability is guaranteed by the generalized Routh criterion. The linearized model of the proposed FA-LESO is established and the design guideline of the observer gains is presented. Compared with the conventional LESO, the proposed FA-LESO can eliminate the steady-state position estimation error without any phase compensation. Meanwhile, it exhibits better high-frequency noise immunity without additional filters being required. The feasibility and effectiveness of the proposed FA-LESO are verified by the comparative experiments on a dual three-phase IPMSM platform.

Index Terms—**Dual three-phase interior permanent magnet synchronous machine (DTP-IPMSM), frequency adaptive, linear extended state observer (LESO), transfer function design.**

I. INTRODUCTION

IN recent years, the multi-phase permanent magnet synchronous motor (PMSM) drive system has been widely studied due to its extra superiorities [1]. For example, since the power of each phase winding decreases as the number of phases increases, the multi-phase PMSM drive system is suitable for high-power applications with low-voltage switching devices, and the lowest order of torque ripple frequency is higher [2]. In addition, as its control degree of freedom is higher than that of its counterpart single three-phase machine, it can continue to operate when one or more phases fail [3]. Based on the aforementioned advantages, multi-phase PMSMs have been widely employed in various applications [4].

Dual three-phase interior PMSM (DTP-IPMSM) is an outstanding candidate for multi-phase machines. Typically, a position sensor is required to obtain accurate rotor position information in vector space decoupling (VSD) control [5], [6] of DTP-IPMSM. To improve the system reliability and reduce the size of the drive system, sensorless control has been extensively studied. The sensorless control can be divided into two categories. The first category is based on high-frequency injection and is mainly employed in the zero- and low-speed

ranges, which utilizes the magnetic anisotropy of the rotor [7]. The second category is based on the fundamental model and commonly employed in medium- and high-speed ranges, which relies on the estimation of flux linkage or back electromotive force (BEMF) [8].

In recent years, the extended state observer (ESO) [9]-[12] has shown great prospects in sensorless control due to its high estimation accuracy, anti-interference capability and robustness to parameter variations [9]. The ESO can be divided into linear ESO (LESO) and nonlinear ESO [13]. Currently, LESO is more widely used than nonlinear ESO due to the convenience of parameter design and stability analysis [14]. However, the transfer function of the conventional LESO (C-LESO) exhibits a second-order low-pass characteristic, which results in the estimated BEMF phase lagging the actual BEMF phase [10]. Although a high bandwidth can mitigate the phase delay, the ability of high-frequency noise suppression is also decreased.

To accurately estimate the BEMF of PMSM, many improved LESOs have been proposed based on the back EMF model in the stationary reference frame or rotating reference frame. In [9], the C-LESO is employed to estimate the BEMFs of IPMSM in the estimated synchronous rotating frame. The speed chattering and phase delay in the sliding mode observer can be mitigated. In [10], and [15], two LESOs in the estimated synchronous frame are used to estimate the BEMF and internal disturbances, respectively. Although the phase delay can be avoided, the LESO in the synchronous rotating frame will be influenced by both speed and position estimation errors due to the unknown rotor position [16].

The LESOs in the stationary reference system have been extensively investigated, which is only affected by speed estimation error. In [11], the bandwidth of LESO is adaptively adjusted according to the motor running frequency to enhance the dynamic performance of the observer, and the phase error in the estimated position is compensated by online calculations. In [12], a LESO with third-order low-pass characteristics was proposed for flux and speed estimation by defining the derivative term of the disturbance as a new state variable. As the bandwidth of the observer is enhanced, the phase delay in the estimated BEMF can be reduced to some extent. However, the fifth and seventh harmonics are dominant in the BEMFs and need to be filtered out by an additional notch filter [17], which leads to increased computational and reduced dynamic performance. In addition, the position estimation error is still

inevitable due to the phase delay of the estimated BEMF. In [18] and [19], a second-order generalized integrator or reduced-order quasi-resonant controller is planted into the internal model of the LESO to reduce the phase error of the estimated BEMF. However, although the phase error can be reduced at relatively low bandwidth, the observer's orders are high due to the addition of an implanted integrator, and the tunning of the parameters is complicated.

In this paper, a frequency adaptive LESO (FA-LESO) is proposed for the sensorless control of the DTP-IPMSM. The proposed observer itself has an ideal frequency adaptive bandpass characteristic, and the phase and amplitude errors in the estimated BEMF can be eliminated without any phase compensation. The high-frequency noise can be effectively suppressed without additional digital filters. Meanwhile, the proposed observer exhibits a simple structure and low order.

This paper is organized as follows: In Section II, the FA-LESO is proposed based on the idea of time-varying gain. In Section III, a comprehensive evaluation of the proposed FA-LESO is presented. In Section IV, the overall sensorless control of DTP-IPMSM based on the FA-LESO is given and the parameter design guideline is presented of the proposed observer based on a linearized model. In Section V, performance comparisons among the C-LESO, GI-LESO, and proposed FA-LESO are performed on a DTP-IPMSM experimental platform. The paper is concluded in Section VI.

II. PROPOSED FA-LESO

In this section, the FA-LESO is proposed based on the idea of gain function backstepping design. The design procedure of FA-LESO is described as follows. Step 1: The unified transfer function of the LESO with time-varying gains is established. Step 2: The transfer function of a second-order complex-coefficient filter is pre-designed based on the desired frequency adaptive characteristic. Step 3: The stability of the pre-designed transfer function is guaranteed based on the generalized Routh array. Step 4: The gains of the proposed observer are configured based on the transfer function in Step 2.

A. Introduction of LESO With Time-Varying-Gains

A typical first-order single input single output system can be expressed as

$$px = f(x,t) + d(t) + b_0 u_0 \tag{1}$$

where p is differential operator, x is the state variable, $f(x, t)$ is known interference, $d(t)$ is unknown interference, u_0 is the system input, b_0 is the coefficient of system input u_0.

If the unknown interference $d(t)$ is extended to a new state, i.e., $x_2=d(t)$, then the original system is equal to the following second-order system:

$$\begin{cases} px_1 = x_2 + b_0 u_0 + f(x_1,t) \\ px_2 = pd(t) \end{cases} \tag{2}$$

where $x_1=x$. Unlike the C-LESO based on constant gain [9]-[18], if the gains of the LESO are considered time-varying, then the LESO can be established as follows:

$$\begin{cases} \varepsilon_1 = \hat{x}_1 - x_1 \\ p\hat{x}_1 = \hat{x}_2 + b_0 u_0 + f(\hat{x}_1,t) - l_1(t)*\varepsilon_1 \\ p\hat{x}_2 = -l_2(t)*\varepsilon_1 \end{cases} \tag{3}$$

where the symbol '*' denotes convolution operation, and the circumflex (ˆ) denotes the estimated value. $l_1(t)$ and $l_2(t)$ represent the gain functions of the LESO. ε_1 represents the estimation error of x_1.

B. LESO with Time-Varying-Gains for BEMF Estimation

According to the well-known VSD model as detailed in [5], [6], the equivalent BEMF model of DTP-IPMSM in the $\alpha\beta$-frame can be expressed as [20]

$$\boldsymbol{u}_{\alpha\beta} = R_s \boldsymbol{i}_{\alpha\beta} + L_q p \boldsymbol{i}_{\alpha\beta} + \boldsymbol{e}_{\alpha\beta} \tag{4}$$

with

$$\boldsymbol{e}_{\alpha\beta} = \omega_e \left[\psi_f + (L_d - L_q) i_d \right] \left[-\sin(\theta_e) \ \cos(\theta_e) \right]^T \tag{5}$$

where $\boldsymbol{u}_{\alpha\beta}$, $\boldsymbol{i}_{\alpha\beta}$, and $\boldsymbol{e}_{\alpha\beta}$ are the vectors of stator voltage, stator current, and equivalent BEMF, respectively. R_s is the stator resistance, L_d and L_q are dq-axis inductances, p is the differential operator, ω_e is the rotor electrical speed, ψ_f is the amplitude of fundamental PM flux linkage, i_d is d-axis current, θ_e is the rotor position angle.

According to (4), the dynamics of DTP-IPMSM in the $\alpha\beta$-frame can be rewritten as follows:

$$p\boldsymbol{i}_{\alpha\beta} = \frac{1}{L_q} \boldsymbol{u}_{\alpha\beta} - \frac{1}{L_q} R_s \boldsymbol{i}_{\alpha\beta} - \frac{1}{L_q} \boldsymbol{e}_{\alpha\beta} \tag{6}$$

The system input vector $\boldsymbol{u}_0$, known interference vector $\boldsymbol{f}$, the state vector $\boldsymbol{x}_1$, and unknown interference vector $\boldsymbol{x}_2$ in (6) can be defined as

$$\begin{cases} b_0 \boldsymbol{u}_0 = \boldsymbol{u}_{\alpha\beta} / L_q \\ \boldsymbol{f} = -R_s \boldsymbol{i}_{\alpha\beta} / L_q = -\mu \boldsymbol{i}_{\alpha\beta} \\ \boldsymbol{x}_1 = \boldsymbol{i}_{\alpha\beta} \\ \boldsymbol{x}_2 = -\boldsymbol{e}_{\alpha\beta} / L_q \end{cases} \tag{7}$$

where $\boldsymbol{x}_1 = [x_{1\alpha} \ x_{1\beta}]$, $\boldsymbol{x}_2 = [x_{2\alpha} \ x_{2\beta}]$, $b_0=1/L_q$, $\boldsymbol{u}_0 = \boldsymbol{u}_{\alpha\beta}$, $\mu=R_s/L_q$.

Then, (6) can be rearranged as

$$p\boldsymbol{x}_1 = b_0 \boldsymbol{u}_{\alpha\beta} - \mu \boldsymbol{x}_1 + \boldsymbol{x}_2 \tag{8}$$

According to (3), the $\alpha\beta$-axis LESOs can be established as follows:

$$\begin{cases} \boldsymbol{\varepsilon}_1 = \hat{\boldsymbol{x}}_1 - \boldsymbol{x}_1 \\ p\hat{\boldsymbol{x}}_1 = \hat{\boldsymbol{x}}_2 + b_0 \boldsymbol{u}_{\alpha\beta} - \mu\hat{\boldsymbol{x}}_1 - l_1(t)*\boldsymbol{\varepsilon}_1 \\ p\hat{\boldsymbol{x}}_2 = -l_2(t)*\boldsymbol{\varepsilon}_1 \end{cases} \tag{9}$$

where $l_1(t)$ and $l_2(t)$ are the gain functions of $\alpha\beta$-axis LESOs.

When the LESOs become stable, the estimated equivalent BEMF vector can be obtained as follows:

$$\hat{\boldsymbol{e}}_{\alpha\beta} = -L_q \hat{\boldsymbol{x}}_2 \tag{10}$$

By subtracting (8) from (9), the estimated current error dynamics can be obtained as

$$\begin{cases} p\boldsymbol{\varepsilon}_1 = \boldsymbol{\varepsilon}_2 - l_1(t)*\boldsymbol{\varepsilon}_1 - \mu\boldsymbol{\varepsilon}_1 \\ p\hat{\boldsymbol{x}}_2 = -l_2(t)*\boldsymbol{\varepsilon}_1 \end{cases} \tag{11}$$

where $\boldsymbol{\varepsilon}_2 = \hat{\boldsymbol{x}}_2 - \boldsymbol{x}_2$.

According to the convolution theorem of the Laplace transform, (11) can be transformed into the frequency domain as

$$\begin{cases} s\boldsymbol{\varepsilon}_1(s) = \boldsymbol{\varepsilon}_2(s) - L_1(s)\boldsymbol{\varepsilon}_1(s) - \mu\boldsymbol{\varepsilon}_1(s) \\ s\hat{\boldsymbol{x}}_2(s) = -L_2(s)\boldsymbol{\varepsilon}_1(s) \end{cases} \quad (12)$$

where $L_1(s)$ and $L_2(s)$ are the Laplace transform of $l_1(t)$ and $l_2(t)$ respectively, and $\boldsymbol{\varepsilon}_1(s) = \hat{\boldsymbol{x}}_1(s) - \boldsymbol{x}_1(s)$, $\boldsymbol{\varepsilon}_2(s) = \hat{\boldsymbol{x}}_2(s) - \boldsymbol{x}_2(s)$.

The first equation of (12) can be further simplified as

$$\boldsymbol{\varepsilon}_1(s) = \frac{1}{s + L_1(s) + \mu}(\hat{\boldsymbol{x}}_2(s) - \boldsymbol{x}_2(s)) \quad (13)$$

According to (10), and by substituting (13) into the second equation of (12), the transfer function from $\boldsymbol{e}_{\alpha\beta}(s)$ to $\hat{\boldsymbol{e}}_{\alpha\beta}(s)$ can be derived as

$$\frac{\hat{\boldsymbol{e}}_{\alpha\beta}(s)}{\boldsymbol{e}_{\alpha\beta}(s)} = \frac{L_2(s)}{s^2 + (\mu + L_1(s))s + L_2(s)} \quad (14)$$

In the C-LESO, when the gains of $l_1(t)$ and $l_2(t)$ in (3) are constant, the (14) can be simplified as

$$\frac{\hat{\boldsymbol{e}}_{\alpha\beta}(s)}{\boldsymbol{e}_{\alpha\beta}(s)} = \frac{l_2}{s^2 + (\mu + l_1)s + l_2} \quad (15)$$

If the two poles of the characteristic equation of (15) are placed at the same point on the left real axis of the complex plane, i.e. l_1 and l_2 of are designed as [9]:

$$\begin{bmatrix} l_1 & l_2 \end{bmatrix}^T = \begin{bmatrix} 2\omega_0 - \mu & \omega_0^2 \end{bmatrix}^T \quad (16)$$

where ω_0 is the bandwidth of the C-LESO, then the transfer function of the C-LESO can be re-obtained as

$$G_{C-LESO}(s) = \frac{\hat{\boldsymbol{e}}_{\alpha\beta}(s)}{\boldsymbol{e}_{\alpha\beta}(s)} = \frac{\omega_0^2}{s^2 + 2\omega_0 s + \omega_0^2} \quad (17)$$

According to (17), the C-LESO exhibits a second-order low-pass characteristic, the phase delay and amplitude error of the estimated BEMF increase with the fundamental frequency [11]. However, according to (14), the frequency characteristic of the proposed LESO can be improved by a proper design of the gain functions $L_1(s)$ and $L_2(s)$.

C. Design of the Desired Observer Transfer Function

The desired observer should have sufficient immunity to harmonics and no phase lag at the fundamental frequency. Based on the requirement, the desired observer transfer function should have similar characteristics to a bandpass filter with the unit gain and zero phase error at the fundamental frequency and deep attenuation outside the fundamental frequency. The transfer function of the observer can be pre-designed, and the gain functions $L_1(s)$ and $L_2(s)$ in (14) should be appropriately configured based on the pre-designed transfer function, which is a reverse design process.

The complex-coefficient filters have been extensively employed for the extraction of the fundamental positive and negative sequences in power grids [21] and current harmonics suppression in PMSM drive systems [22]. The uniform transfer function of the filter is [23]

$$G_{CCF}(s) = \frac{N(s)}{(s - j\hat{\omega}_e)D(s) + N(s)} \quad (18)$$

where $N(s)$ and $D(s)$ can be designed flexibly.

The response of (18) at the estimated fundamental frequency $\hat{\omega}_e$ can be calculated as

$$\begin{aligned} G_{CCF}(+j\hat{\omega}_e) &= \left. \frac{N(s)}{(s - j\hat{\omega}_e)D(s) + N(s)} \right|_{s=j\hat{\omega}_e} \\ &= \frac{N(j\hat{\omega}_e)}{(j\hat{\omega}_e - j\hat{\omega}_e)D(j\hat{\omega}_e) + N(j\hat{\omega}_e)} = 1\angle 0^0 \end{aligned} \quad (19)$$

According to (19), the desired signal at the estimated fundamental frequency $\hat{\omega}_e$ can be extracted without amplitude and phase errors.

The transfer functions (14) and (18) are very similar if $N(s)$ and $D(s)$ are set as

$$\begin{aligned} N(s) &= k_1 + k_2 s \\ D(s) &= s \end{aligned} \quad (20)$$

Then, the transfer function of the second-order complex-coefficient-filter can be obtained as

$$G_{CCF}(s) = \frac{k_1 + k_2 s}{s^2 - j\hat{\omega}_e s + k_1 + k_2 s} \quad (21)$$

Fig. 1 shows the frequency characteristic of $G_{CCF}(s)$ with different k_1, where the estimated speed $\hat{\omega}_e = 50$ Hz and $k_2 = 100$ π. Fig. 2 shows the frequency characteristic of $G_{CCF}(s)$ with different k_2, where the estimated speed $\hat{\omega}_e = 50$ Hz and $k_1 = 10$ π. k_2 is positively correlated with the filtering effect of the designed transfer function.
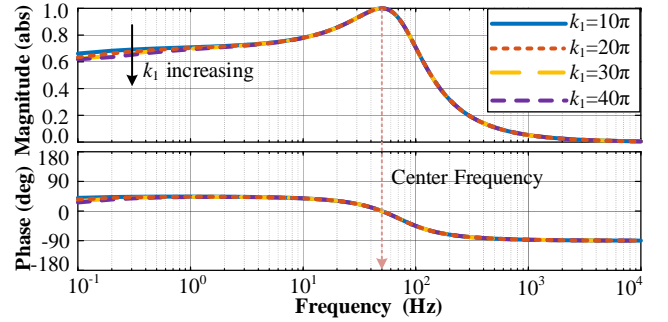
Fig. 1. Bode diagram of the designed transfer function with different k_1, where the estimated speed $\hat{\omega}_e = 50$ Hz and $k_2 = 100$ π.
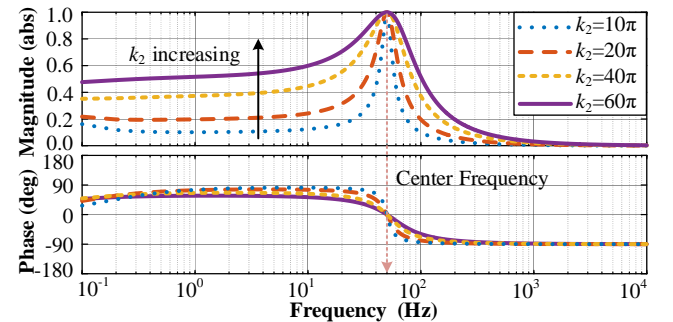
Fig. 2. Bode diagram of the designed transfer function with different k_2, where the estimated speed $\hat{\omega}_e = 50$ Hz and $k_1 = 10$ π.

The stability of the designed transfer function $G_{CCF}(s)$ should be guaranteed. The characteristic polynomial of (21) is

$$\lambda(s) = s^2 + (k_2 - j\hat{\omega}_e)s + k_1 \quad (22)$$

According to [24], the generalized Routh array for (22) is given in TABLE I.

s^2	a_0	b_1	a_2
s^1	a_1	b_2	
	$b_1^{(1)}$	$a_2^{(1)}$	
s^0	$a_2^{(2)}$		

where

$$a_0 = 1, a_1 = k_2, a_2 = k_1, b_0 = 0, b_1 = -\hat{\omega}_e, b_2 = 0.$$

$$a_2^{(1)} = a_1 a_2 = k_1 k_2, b_1^{(1)} = a_1 b_1 - a_0 b_2 = -\hat{\omega}_e k_2 \quad (23)$$

$$a_2^{(2)} = a_1 a_2^{(1)} + b_1^{(1)} b_2 = k_1 k_2$$

The stability condition of $G_{CCF}(s)$ is

$$a_0 > 0, a_1 > 0, a_2^{(2)} > 0 \quad (24)$$

When $k_1 > 0$ and $k_2 > 0$, the stability condition in (24) is satisfied.

D. Introduction of Proposed FA-LESO

In this section, a novel FA-LESO is proposed, whose transfer function is configured to be the same as $G_{CCF}(s)$ in (21). The gain functions $L_1(s)$ and $L_2(s)$ in (14) can be designed as

$$L_1(s) = -j\hat{\omega}_e - \mu, L_2(s) = k_1 + k_2 s \quad (25)$$

Thus, the transfer function of the proposed FA-LESO can be derived as

$$G_{FA-LESO}(s) = \frac{\hat{e}_{\alpha\beta}(s)}{e_{\alpha\beta}(s)} = \frac{k_1 + k_2 s}{s^2 - j\hat{\omega}_e s + k_1 + k_2 s} \quad (26)$$

According to (9) and (25), the α-axis FA-LESO can be derived in the frequency domain as follows:

$$\begin{cases} E_{1\alpha}(s) = \hat{X}_{1\alpha}(s) - X_{1\alpha}(s) \\ \hat{X}_{1\alpha}(s) = \frac{1}{s}[\hat{X}_{2\alpha}(s) + b_0 U_\alpha(s) + F_\alpha(s) \\ \quad + \mu E_{1\alpha}(s) - \hat{\omega}_e E_{1\beta}(s)] \\ \hat{X}_{2\alpha}(s) = -(\frac{k_1}{s} + k_2) E_{1\alpha}(s) \end{cases} \quad (27)$$

Similarly, the β-axis FA-LESO can be derived in the frequency domain as follows:

$$\begin{cases} E_{1\beta}(s) = \hat{X}_{1\beta}(s) - X_{1\beta}(s) \\ \hat{X}_{1\beta}(s) = \frac{1}{s}[\hat{X}_{2\beta}(s) + b_0 U_\beta(s) + F_\beta(s) \\ \quad + \mu E_{1\beta}(s) + \hat{\omega}_e E_{1\alpha}(s)] \\ \hat{X}_{2\beta}(s) = -(\frac{k_1}{s} + k_2) E_{1\beta}(s) \end{cases} \quad (28)$$

According to (27) and (28), the control block diagram of the proposed FA-LESO for the $\alpha\beta$-axis can be obtained as shown in Fig. 3. The reference voltages u_a^* and u_β^*, the sampled currents i_α and i_β, and the estimated angular velocity $\hat{\omega}_e$ are employed as the inputs of the FA-LESO. The outputs of the FA-LESO are the estimated equivalent BEMFs.

The low-speed limit depends on the noise of the estimated speed and rotor position error resulting from the parameters mismatch, nonlinearity of the inverter, and non-sinusoidal BEMF. In the proposed observer, the voltage command is used

as input; however, it is not equal to the actual output voltage due to the nonlinearity of the inverter, which will inevitably affect the estimated rotor position based on ESOs for BEMF, especially at the low speed where the BEMF is relatively small [25]. Meanwhile, accurate stator resistance is also critical for low-speed operation. To extend the low-speed operation limit, the methods of reducing the speed loop bandwidth [25], dedicated inverter nonlinearity compensation [26] or directly measuring the output voltage [27] can be employed. However, this will not be the focus of this paper.
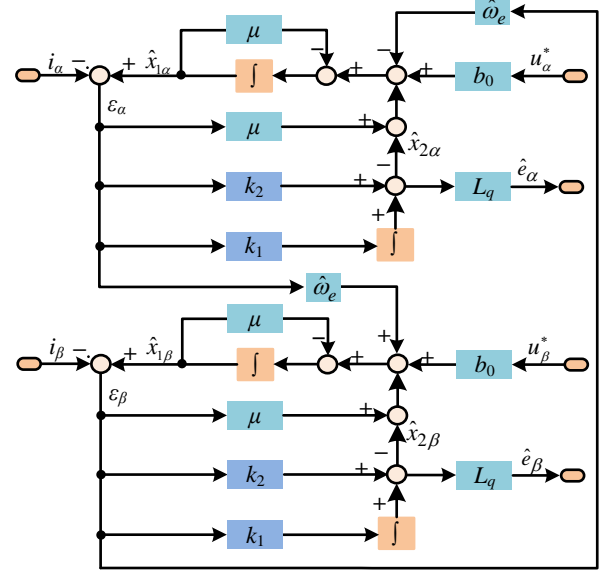
Fig. 3. Structure diagram of the proposed FA-LESO for $\alpha\beta$-axis.

III. EVALUATION OF FA-LESO

In this section, the frequency characteristics, complexity, and robustness of parameter mismatches of the proposed FA-LESO are evaluated by comparison with the C-LESO and the GI-LESO. The transfer functions and parameters settings of the C-LESO, the GI-LESO and the FA-LESO are listed in TABLE II. The GI-LESO transfer function can be expressed as

$$G_{GI-LESO}(s) = \frac{G(s) + \omega_0^2}{s^2 + 2\omega_0 s + G(s) + \omega_0^2} \quad (29)$$

where $G(s)$ is the generalized integrator that expressed as

$$G(s) = \frac{2K_r \omega_c s}{s^2 + 2\omega_c s + \hat{\omega}_e^2} \quad (30)$$

where K_r and ω_c are the gain and attenuation coefficients of the integrator, respectively.

Observers	Transfer Function	Parameters
C-LESO	$\dfrac{\omega_0^2}{s^2 + 2\omega_0 s + \omega_0^2}$	$\omega_0 = 500\pi.$
GI-LESO	$\dfrac{G(s) + \omega_0^2}{s^2 + 2\omega_0 s + G(s) + \omega_0^2}$	$\omega_0 = 500\pi, K_r = 2 \times (\omega_0)^2,$ $\omega_c = \pi, \hat{\omega}_e = 100\pi.$
FA-LESO	$\dfrac{k_1 + k_2 s}{s^2 - j\hat{\omega}_e s + k_1 + k_2 s}$	$k_1 = 10\pi, k_2 = 100\pi,$ $\hat{\omega}_e = 100\pi.$

A. Evaluation of Frequency Characteristics and Complexity

Fig. 4 shows the bode diagrams of the C-LESO, the GI-LESO, and the proposed FA-LESO. According to Fig. 4, the C-LESO exhibits a second-order lowpass characteristic, which leads to an increase in the steady-state position error with the motor running frequency. The high bandwidth can reduce the phase error; however, the suppression effect on the noise will be weakened. In the GI-LESO, although the high gain of the generalized integrator can help reduce the steady-state phase error to some extent, which may lead to instability of the control algorithm [11]. Fortunately, the proposed observer exhibits a frequency adaptive bandpass characteristic, ensuring that the proposed FA-LESO can eliminate the steady-state position error. In addition, it exhibits better noise immunity than the C-LESO and GI-LESO.

As far as the complexity is concerned, the order of the C-LESO and the proposed observer is 2. In contrast, the order of the GI-LESO is 4 due to the additional implanted integrator. Therefore, the proposed observer has a lower order than the GI-LESO. Moreover, if the suppression of low-frequency noise is not considered, only the parameter k_2 related to high-frequency noise suppression needs to be tuned in the proposed observer. However, the parameters ω_0, ω_c, and K_r in the GI-LESO need to be adjusted to satisfy the stability. Therefore, the parameters of the proposed observer are more easily tuned than the GI-LESO.
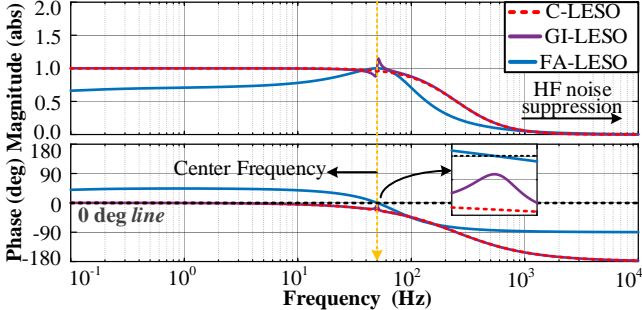
Fig. 4. Bode diagrams of the C-LESO, GI-LESO, and proposed FA-LESO.

B. Evaluation of Parameter Mismatches

The estimated nominal BEMF can be derived as

$$\hat{e}_{\alpha\beta}^{\text{nom}}(s) = G_{BEMF}(s)e_{\alpha\beta}^{\text{nom}}(s) \tag{31}$$

where the symbol 'nom' denotes nominal value, and $G_{BEMF}(s)$ represents the transfer function of the BEMF observer. The estimated equivalent nominal BEMF is determined by $G_{BEMF}(s)$ and the nominal BEMF $e_{\alpha\beta}^{nom}$. The $G_{BEMF}(s)$ could be any one of the transfer functions in TABLE II and the nominal BEMF $e_{\alpha\beta}^{nom}$ can be obtained by

$$p\boldsymbol{i}_{\alpha\beta} = \frac{1}{L_q^{\text{nom}}}\boldsymbol{u}_{\alpha\beta} - \frac{1}{L_q^{\text{nom}}}R_s^{\text{nom}}\boldsymbol{i}_{\alpha\beta} - \frac{1}{L_q^{\text{nom}}}\boldsymbol{e}_{\alpha\beta}^{\text{nom}} \tag{32}$$

Then, the resulting BEMF error $\Delta\boldsymbol{e}_{\alpha\beta}$ can be calculated by subtracting (32) from (6) as

$$\Delta\boldsymbol{e}_{\alpha\beta} = \boldsymbol{e}_{\alpha\beta} - \boldsymbol{e}_{\alpha\beta}^{\text{nom}} = -(\Delta L_q p + \Delta R_s)\boldsymbol{i}_{\alpha\beta} \tag{33}$$

where $\Delta L_q = L_q - L_q^{\text{nom}}$, $\Delta R_s = R_s - R_s^{\text{nom}}$. L_q^{nom} and R_s^{nom} are the nominal parameters, while L_q and R_s are the real parameters.

The $\Delta\boldsymbol{e}_{\alpha\beta}$ can be transformed into the frequency domain as

$$\Delta\boldsymbol{e}_{\alpha\beta}(s) = \boldsymbol{e}_{\alpha\beta}(s) - \boldsymbol{e}_{\alpha\beta}^{\text{nom}}(s) = -(\Delta L_q s + \Delta R_s)\boldsymbol{i}_{\alpha\beta}(s) \tag{34}$$

According to (31), the estimated equivalent BEMF error $\Delta\hat{\boldsymbol{e}}_{\alpha\beta}(s)$ can be expressed as

$$\Delta\hat{\boldsymbol{e}}_{\alpha\beta}(s) = \hat{\boldsymbol{e}}_{\alpha\beta}(s) - \hat{\boldsymbol{e}}_{\alpha\beta}^{\text{nom}}(s) = G_{BEMF}(s)\Delta\boldsymbol{e}_{\alpha\beta}(s) \tag{35}$$

As shown in TABLE II, the bandwidth ω_0 of C-LESO is usually much larger than the fundamental frequency $\hat{\omega}_e$, and the amplitude of C-LESO at the fundamental frequency is

$$\left|G_{C-LESO}(j\hat{\omega}_e)\right| \approx 1 \tag{36}$$

According to (30), since $\left|G(j\hat{\omega}_e)\right| \to +\infty$, the amplitude of the GI-LESO in (29) at the fundamental frequency is

$$\left|G_{GI-LESO}(j\hat{\omega}_e)\right| \approx 1 \tag{37}$$

According to (26), the amplitude of FA-LESO at the fundamental frequency is

$$\left|G_{FA-LESO}(j\hat{\omega}_e)\right| = 1 \tag{38}$$

According to (36) - (38), $\Delta\hat{\boldsymbol{e}}_{\alpha\beta}(s)$ caused by parameter mismatches are almost the same in the three observers. For the proposed FA-LESO, $\Delta\hat{\boldsymbol{e}}_{\alpha\beta}(s)$ can be calculated by substituting (34) and (38) into (35) as

$$\Delta\hat{\boldsymbol{e}}_{\alpha\beta} = -(\Delta L_q p + \Delta R_s)\boldsymbol{i}_{\alpha\beta} \tag{39}$$

Then, (39) can be transformed into the estimated synchronous coordinate system as

$$\Delta\hat{\boldsymbol{e}}_{dq} = -\Delta R_s\hat{\boldsymbol{i}}_{dq} - j\Delta L_q\hat{\omega}_e\hat{\boldsymbol{i}}_{dq} \tag{40}$$

The position estimation error caused by the parameter mismatches can be deduced as

$$\Delta\theta_{par} = \arctan(\frac{\Delta e_d}{E_{ex} + \Delta e_q}) \tag{41}$$

where E_{ex} is the amplitude of equivalent BEMF.

Therefore, by substituting (40) into (41), the position estimation errors caused by stator resistance or inductance mismatches can be calculated respectively as

$$\Delta\theta_{\Delta R_s} = \arctan(\frac{-\Delta R_s\hat{i}_d}{E_{ex} - \Delta R_s\hat{i}_q}) \tag{42}$$

$$\Delta\theta_{\Delta L_q} = \arctan(\frac{\Delta L_q\hat{i}_q}{E_{ex}/\hat{\omega}_e - \Delta L_q\hat{i}_d}) \tag{43}$$

As can be seen in (42), $\Delta\theta_{\Delta Rs}$ decreases as speed increases for a given stator resistance deviation and estimated d-axis current $\hat{i}_d$. If $\hat{i}_d$ is controlled to zero, the $\Delta\theta_{par}$ will be unaffected by the stator resistance deviation. However, if $\hat{i}_d$ is not controlled to zero, the stator resistance deviation will inevitably lead to position estimation error. For the q-axis inductance deviation, as can be seen in (43), $\Delta\theta_{\Delta Lq}$ is independent of the speed while it is related to the estimated q-axis current. Under no-load conditions, it will be unaffected by the q-axis inductance deviation. However, it will inevitably lead to position estimation error under load conditions.

The parameter design of the observer is crucial to optimize the sensorless control performance. In this section, a sensorless control strategy based on the proposed FA-LESO for DTP-IPMSM drives is presented, and a small-signal linearized model is established, which facilitates the parameter design of the proposed observer.

A. Overall Sensorless Control Strategy

The normalized quadrature phase-locked loop (QPLL) in Fig. 5 is usually used to estimate the rotor position and speed. The normalized $\hat{e}_\alpha$ and $\hat{e}_\beta$ are as the inputs, k_p and k_i are parameters of the proportional-integral (PI) estimator, and the output of QPLL is the estimated rotor speed and position. The overall block diagram of the sensorless control for DTP-IPMSM drives based on the proposed FA-LESO is shown in Fig. 6.

Fig. 5. Block diagram of the QPLL.

Fig. 6. Overall block diagram of the sensorless control for DTP-IPMSM drives based on the proposed FA-LESO.

In Fig. 6, the DTP-IPMSM consists of two sets of three-phase windings with isolated neutral points, where the first set is phase-ABC and the second set is phase-XYZ. The dual space vector PWM (SVPWM) strategy is adopted for PWM generation, where the conventional SVPWM strategy is applied to each single three-phase voltage source inverter (VSI). The harmonic controller (HC) is employed to suppress the dominant 5th and 7th current harmonics in the $z1z2$-frame [28]. The VSD matrix T_{VSD}, the conventional Park matrix T_{dq}, and the matrix T_{dqz} are detailed in the [6]. By the matrix T_{VSD}, the fundamental and $12k\pm1$th ($k=1,2,3...$) order harmonics in the ABC-XYZ-frame are mapped into the $\alpha\beta$-frame, while $6k\pm1$th (k=1,3,5...) order harmonics are mapped into the $z1z2$-frame. Therefore, unlike the general three-phase IPMSM, the 11th and 13th

harmonics are dominant in the $\alpha\beta$-frame for the DTP-IPMSM. In addition, if the DTP-IPMSM is treated as two individual single three-phase IPMSMs based on the double d-q model [6], the 5th and 7th harmonics will be dominant in the $\alpha\beta$-frame of each three-phase winding [29]. Therefore, the VSD control strategy is used to achieve BEMF estimation of DTP-IPMSM, which can naturally avoid the interference of the 5th and 7th BEMF harmonics. Nevertheless, the proposed observer has a strong immunity to the dominant 5th and 7th BEMF harmonics in general single three-phase IPMSMs, which will also be demonstrated in the experiments.

B. Linearized Model and Parameter Design

In the proposed observer in Fig. 6, the parameters k_1 and k_2 in Fig. 3 and the parameters k_p and k_i in the QPLL in Fig. 5 need to be designed. These parameters will be designed based on the linearized model.

The actual equivalent BEMF $\boldsymbol{e}_{\alpha\beta}$ can be expressed as

$$\boldsymbol{e}_{\alpha\beta} = -E_{ex}\sin(\theta_e) + jE_{ex}\cos(\theta_e) \tag{44}$$

The estimated equivalent BEMF $\hat{\boldsymbol{e}}_{\alpha\beta}$ can be expressed as

$$\hat{\boldsymbol{e}}_{\alpha\beta} = -\hat{E}_{ex}\sin(\hat{\theta}_k) + j\hat{E}_{ex}\cos(\hat{\theta}_k) \tag{45}$$

where $\hat{E}_{ex}$ and $\hat{\theta}_k$ are the amplitude and phase of $\hat{\boldsymbol{e}}_{\alpha\beta}$, respectively. The phase $\hat{\theta}_k$ can be calculated as

$$\hat{\theta}_k = -\arctan(\hat{e}_\alpha / \hat{e}_\beta) \tag{46}$$

The first-order time differentiation of (46) will be

$$\dot{\hat{\theta}}_k = (\hat{e}_\alpha \dot{\hat{e}}_\beta - \dot{\hat{e}}_\alpha \hat{e}_\beta) / \hat{E}_{ex}^2 \tag{47}$$

The second-order time differentiation of (46) is

$$\ddot{\hat{\theta}}_k = (\hat{e}_\alpha \ddot{\hat{e}}_\beta - \ddot{\hat{e}}_\alpha \hat{e}_\beta) / \hat{E}_{ex}^2 \tag{48}$$

The $\hat{\boldsymbol{e}}_{\alpha\beta}$ in the time domain can be calculated from (26) as

$$\ddot{\hat{\boldsymbol{e}}}_{\alpha\beta} + (k_2 - j\hat{\omega}_e)\dot{\hat{\boldsymbol{e}}}_{\alpha\beta} + k_1\hat{\boldsymbol{e}}_{\alpha\beta} = k_1\boldsymbol{e}_{\alpha\beta} + k_2\dot{\boldsymbol{e}}_{\alpha\beta} \tag{49}$$

Substituting (49) into (48) and then (48) can be simplified as

$$\ddot{\hat{\theta}}_k = \frac{E_{ex}}{\hat{E}_{ex}}[k_1\sin(\theta_e - \hat{\theta}_k) + k_2\omega_e\cos(\theta_e - \hat{\theta}_k)] - k_2\dot{\hat{\theta}}_k \tag{50}$$

Under the condition $\theta_e - \hat{\theta}_k \to 0$, $E_{ex} \to \hat{E}_{ex}$, by the small signal approximation theory, (50) can be re-derived as [30]

$$\ddot{\hat{\theta}}_k = k_1(\theta_e - \hat{\theta}_k) + k_2\dot{\theta}_e - k_2\dot{\hat{\theta}}_k \tag{51}$$

Therefore, the transfer function from θ_e to $\hat{\theta}_k$ is

$$\frac{\hat{\theta}_k(s)}{\theta_e(s)} = \frac{k_1 + k_2 s}{s^2 + k_2 s + k_1} \tag{52}$$

In addition, the position error signal $f(\Delta\theta_e)$ in QPLL in Fig. 5 can be obtained as

$$f(\Delta\theta_e) = -\frac{\hat{e}_\alpha}{\sqrt{\hat{e}_\alpha^2 + \hat{e}_\beta^2}}\cos(\hat{\theta}_e) - \frac{\hat{e}_\beta}{\sqrt{\hat{e}_\alpha^2 + \hat{e}_\beta^2}}\sin(\hat{\theta}_e) \tag{53}$$

$$= \sin(\Delta\theta_e)$$

where $\Delta\theta_e = \hat{\theta}_k - \hat{\theta}_e$. Therefore, the closed-loop transfer function from $\hat{\theta}_k$ to $\hat{\theta}_e$ can be obtained as

$$\frac{\hat{\theta}_e(s)}{\hat{\theta}_k(s)} = \frac{k_i + k_p s}{s^2 + k_p s + k_i} \tag{54}$$

According to (52) and (54), the overall linearized model of

the rotor position estimator based on the proposed FA-LESO and the cascaded QPLL can be illustrated in Fig. 7.

Fig. 7. Overall small-signal linearized model of rotor position estimator based on the proposed observer and the cascaded QPLL.

According to (52) and (54), the closed-loop transfer function from θ_e to $\hat{\theta}_e$ can be obtained as

$$\frac{\hat{\theta}_e(s)}{\theta_e(s)} = \frac{k_1 + k_2 s}{s^2 + k_2 s + k_1} \frac{k_i + k_p s}{s^2 + k_p s + k_i} \tag{55}$$

Furthermore, (55) can be rewritten as

$$\frac{\hat{\theta}_e(s)}{\theta_e(s)} = \frac{k_1 + k_2 s}{(s+a)(s+b)} \frac{k_i + k_p s}{s^2 + k_p s + k_i} \tag{56}$$

where

$$\begin{cases} ab = k_1 \\ a+b = k_2 \end{cases} \tag{57}$$

Define $b = k_i/k_p$, and apply the zero-pole elimination principle to simplify (56) to a third-order system as

$$\frac{\hat{\theta}_e(s)}{\theta_e(s)} = \frac{k_1 + k_2 s}{(s+a)} \frac{k_p}{s^2 + k_p s + k_i} \tag{58}$$

The characteristic polynomial of (58) can be configured as

$$p(s) = (s + \rho\zeta\omega_n)(s^2 + 2\zeta\omega_n s + \omega_n^2) \tag{59}$$

where ζ is the damping ratio and ω_n is the natural oscillation frequency, ρ is the coefficient of the system.

Comparing (58) and (59), it leads to

$$\begin{cases} k_p = 2\zeta\omega_n, k_i = \omega_n^2 \\ a = \rho\zeta\omega_n, b = \omega_n/(2\zeta) \end{cases} \tag{60}$$

According to (57) and (60), k_1 and k_2 can be obtained as

$$\begin{cases} k_1 = \rho\omega_n^2 / 2 \\ k_2 = \omega_n/(2\zeta) + \rho\zeta\omega_n \end{cases} \tag{61}$$

The characteristic polynomial (59) has three poles, which are

$$s_{1,2} = -\zeta\omega_n \pm j\omega_n\sqrt{(1-\zeta^2)}, s_3 = -\rho\zeta\omega_n \tag{62}$$

If $\zeta > 0$, $\omega_n > 0$, and $\rho > 0$, the real parts of the three poles are negative, the stability of the observer and the QPLL can be guaranteed. The dominant pole approximation method is used to approximate the third-order system as a second-order system [31]. The real part of the pole s_3 should be at least five times larger than the real part of poles $s_{1,2}$, e.g. $\rho \geq 5$. In this paper, ρ is chosen as 5. The bode diagram of (58) with different ω_n is shown in Fig. 8, where ζ is usually chosen as 0707. As can be seen that the bandwidth of the observer increases when the natural frequency ω_n increases; however, the filtering capability decreases. To achieve a well-damped dynamic response and damped effect, ω_n is chosen as 100π rad/s in this paper.

Fig. 8. Bode diagram of the linearized model of Fig. 7.

V. EXPERIMENTAL RESULTS

Fig. 9 shows the DTP-IPMSM test platform based on TI's DSP processor TMS320F28335. The inverter consists of two single three-phase VSIs with the same common DC bus. With the aid of accurate rotor position information from an encoder, the accuracy of the position estimate is verified. In this paper, the encoder is used to obtain the actual rotor position, and the driver starts the DTP-IPMSM and switches to sensorless operation at the target speed. The inverter-I is used to drive the prototype DTP-IPMSM, while the inverter-II is used to drive the load machine. For simplicity, the current control method with $i_d^* = 0$ is employed in this paper. The parameters of the prototype DTP-IPMSM are listed in TABLE III. The parameters of the C-LESO and the GI-LESO are selected as described in Section III. (A). The parameters of the proposed FA-LESO are selected as described in Section III. (A). For fairness, the same QPLL parameters and current loop parameters are employed in the experimental tests, and there are no phase compensation measures or additional digital filters.

Fig. 9. Experimental setup for prototype DTP-IPMSM drive system.

TABLE III
PARAMETERS OF PROTOTYPE DTP-IPMSM

Parameters	Value	Parameters	Value
Resistance(Ω)	0.15	d-axis inductance(mH)	4.336
Flux linkage (Wb)	0.0785	q-axis inductance(mH)	5.841
Pole pairs	5	Rated power(W)	1200
Rated current (A)	12	Rated speed (r/min)	600
DC link voltage (V)	80	PWM frequency (Hz)	10 k

A. Steady-State Test Under No Load

In this section, the steady-state performance of the C-LESO, the GI-LESO, and the proposed FA-LESO are compared. The prototype DTP-IPMSM runs in speed control mode under no load. Fig. 10, Fig. 11, and Fig. 12 show the actual and estimated

rotor positions and position estimation errors of the C-LESO, GI-LESO, and FA-LESO at 300 r/min, 600 r/min, and 840 r/min, respectively. The field-weakening control is engaged for d-axis current reference generation [32]. The corresponding operating frequencies are 25 Hz, 50 Hz, and 70 Hz, respectively. In Fig. 10 (a), Fig. 11 (a) and Fig. 12 (a), the rotor position estimation error increases as speed increases in the C-LESO; the mean value of the position estimation errors at 300 r/min, 600 r/min, and 840 r/min are 14.0 deg, 23.0 deg, and 34.0 deg, respectively. In Fig. 10 (b), Fig. 11 (b) and Fig. 12 (b), the mean value of the position estimation error with the GI-LESO

are 7 deg, 10 deg, and 12 deg, respectively. This shows that the rotor position estimation error is reduced to some extent in the GI-LESO if compared with C-LESO, which is consistent with the analysis of the Bode diagram in Section III. (A). However, according to Fig. 10 (c), Fig. 11 (c), and Fig. 12 (c), the mean values of the position estimation errors with the proposed FA-LESO are all nearly to 0 rad, and the fluctuation of the errors are within 2.3 deg. Therefore, compared with the C-LESO and the GI-LESO, the proposed FA-LESO can accurately estimate the equivalent BEMF without phase delay.
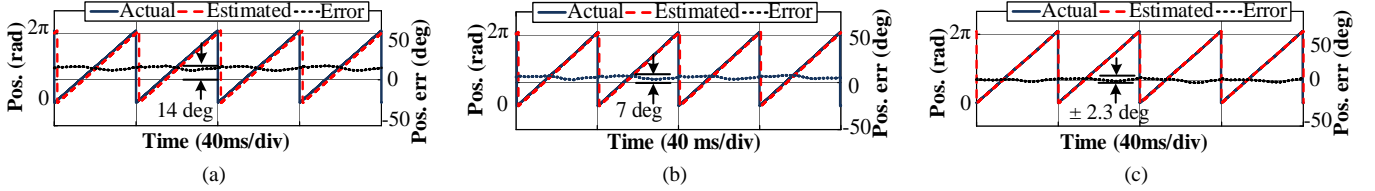
Fig. 10. Steady-state experimental results for no load at 300 r/min (25 Hz). (a) C-LESO. (b) GI-LESO. (c) FA-LESO.
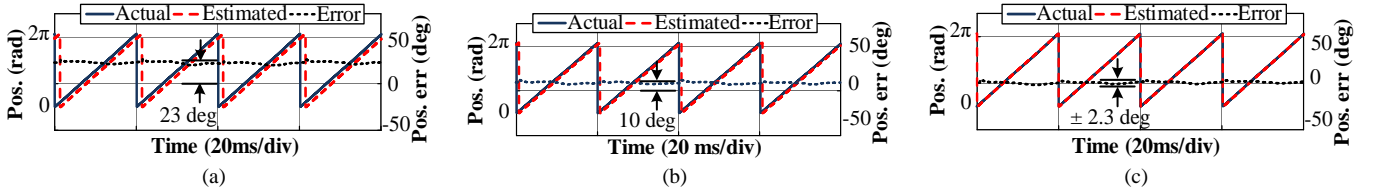
Fig. 11. Steady-state experimental results for no load at 600 r/min (50 Hz). (a) C-LESO. (b) GI-LESO. (c) FA-LESO.
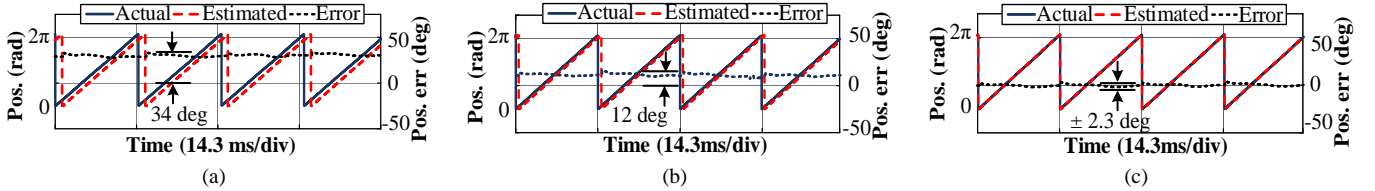
Fig. 12. Steady-state experimental results for no load at 840 r/min (70 Hz). (a) C-LESO. (b) GI-LESO. (c) FA-LESO.

B. Steady-State Test Under Full-Load

In this section, Fig. 13 - Fig. 15 demonstrate the estimated equivalent BEMFs, actual and estimated position, and position estimation error at different speeds under full load. The proposed FA-LESO shows better performance than C-LESO and GI-LESO, which is similar to the results in the steady-state test under no load. Therefore, it will not be introduced in detail for simplicity. In addition, the harmonic analysis of the α-axis estimated equivalent BEMF and the harmonics attenuation of the C-LESO, the GI-LESO, and the proposed FA-LESO will also be included and compared.

Due to the relatively low levels of the 11th and 13th BEMF harmonics in the DTP-IPMSM, to adequately demonstrate the harmonics attenuation of the proposed observer FA-LESO, the DTP-IPMSM is treated as two individual sets of single three-phase PMSMs [6] and the LESOs are only applied to the first set, where the 5th and 7th BEMF harmonics are dominant.

Fig. 13 shows the test results of the first set of windings at 300 r/min under a half-rated load. The estimated equivalent BEMFs with the C-LESO in Fig. 13 (a) and GI-LESO in Fig. 13 (b) are seriously deteriorated due to the dominant 5th and 7th BEMF harmonics, which lead to the 6th harmonic in the estimated position. The 5th and 7th harmonics with the C-

LESO are 5.4 % and 5.9 % respectively, and the 5th and 7th harmonics with the GI-LESO are 3.6 % and 4.0 % respectively. Compared with the C-LESO and GI-LESO, the 5th and 7th harmonics with the proposed FA-LESO are reduced to 0.8 % and 0.7 % in Fig. 13 (c), respectively.

According to Fig. 11 (a), the C-LESO has a large position estimation error at 600 r/min; therefore, the half-rated load test cannot be completed. To continue the comparison among the C-LESO, GI-LESO and the proposed FA-LESO, the load is reduced to 40% of the rated value at 600 r/min and the test results are shown in Fig. 14. In Fig. 14 (a) and Fig. 14 (b), the 5th and 7th harmonics are still not sufficiently attenuated by C-LESO and GI-LESO, where the 5th and 7th harmonics with the C-LESO are 4.1% and 4.5%, respectively, the 5th and 7th harmonics with the GI-LESO are 2.7% and 2.9%, respectively. However, the 5th and 7th harmonics with the proposed observer are significantly reduced to 0.6 % and 0.7 % in Fig. 14 (c), respectively.

Fig. 15 shows the test results of the DTP-IPMSM with VSD control strategy at 600 r/min under 80 % of the rated load. According to Fig. 15 (a) - Fig. 15 (c), the 5th and 7th harmonics with the three observers are negligible, which is consistent with the VSD control theory where the 5th and 7th harmonics

are all mapped to harmonic sub-plane [5]. It is noteworthy that the estimated BEMF harmonics with the FA-LESO are lower than the other two methods. Therefore, the proposed observer is superior to the C- ESO and GI-LESO in terms of harmonics attenuation.
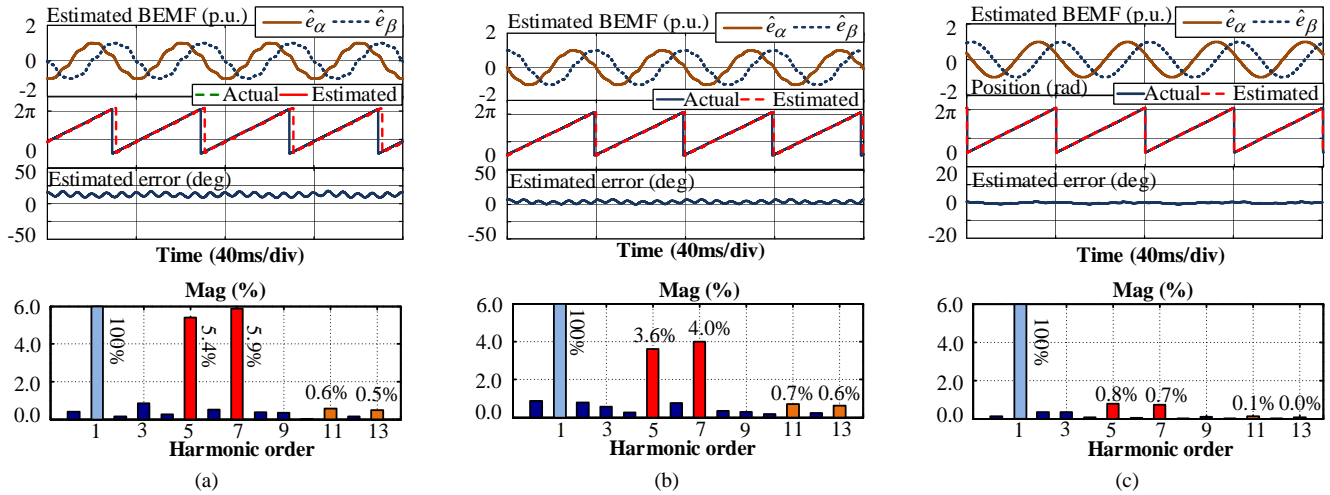
Fig. 13. The steady-state test results of the first set of windings at 300 r/min (25 Hz) under half-rated load. (a) C-LESO. (b) GI-LESO. (c) FA-LESO.
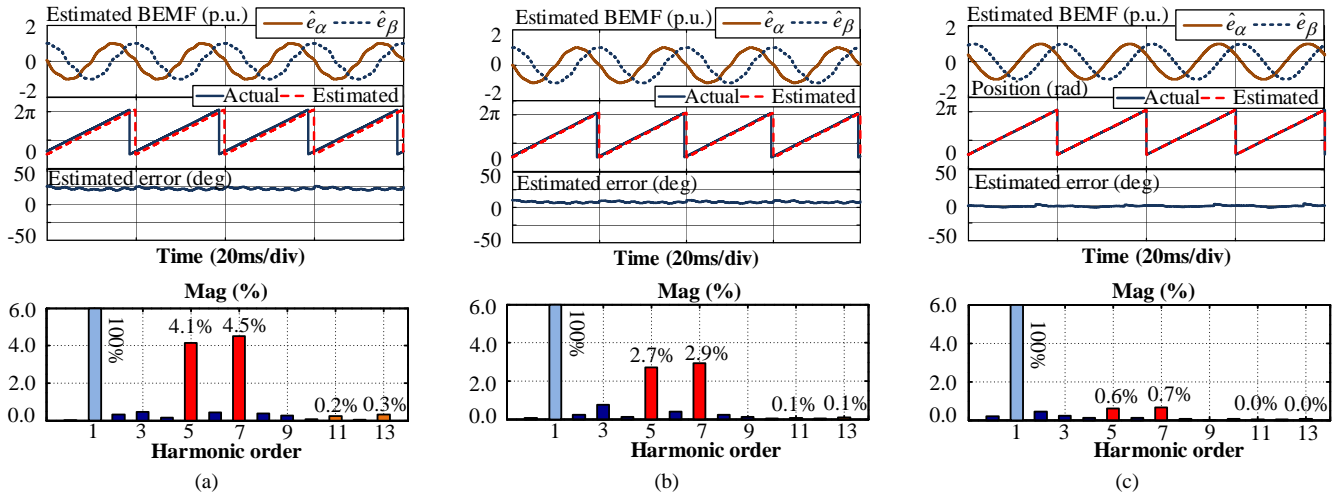
Fig. 14. The steady-state test results of the first set of windings at 40% of rated load and 600 r/min (50 Hz). (a) C-LESO. (b) GI-LESO. (c) FA-LESO.
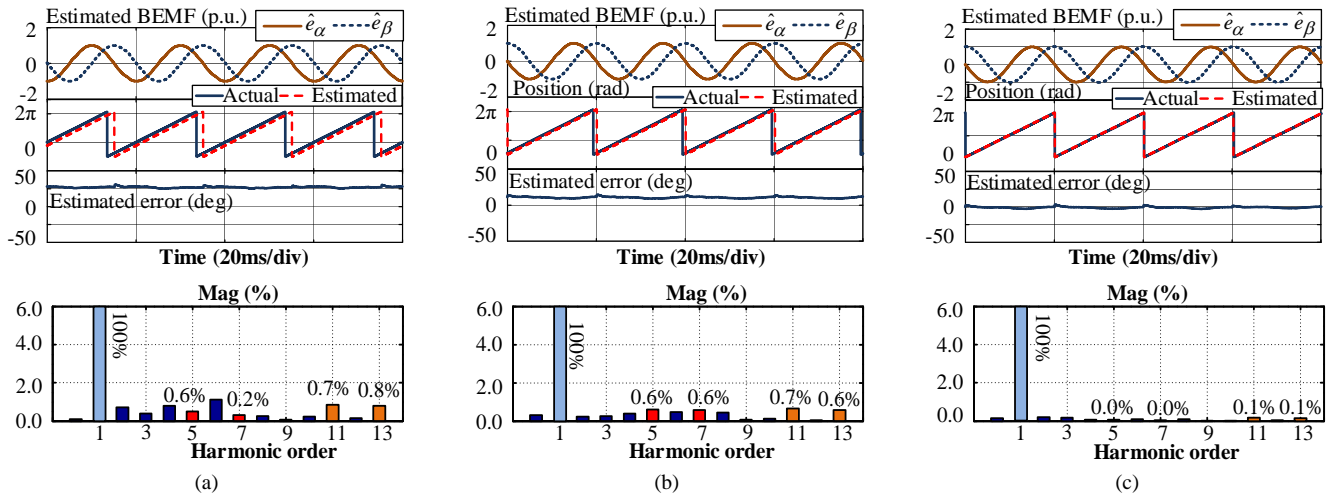
Fig. 15. The steady-state test results of the DTP-IPMSM with VSD control strategy at 80% of rated load and 600 r/min (50 Hz). (a) C-LESO. (b) GI-LESO. (c) FA-LESO.

C. Transient Test

The transient performance of the C-LESO, the GI-LESO, and the proposed FA-LESO are compared by the speed ramp test and the load step test in this section.

In the speed ramp test, the DTP-IPMSM runs at no-load and the speed command changes in the sequence of 300-600-840-600-300 r/min. The actual and estimated speeds, speed

estimation error, and position estimation error are presented. In Fig. 16 (a) - Fig. 16 (c), the speed estimation performance is well achieved, and the largest speed estimation errors are 13 r/min. In the C-LESO and the GI-LESO, the position estimation errors include steady-state and dynamic errors during acceleration and deceleration, while in the FA-LESO, only dynamic errors appear during acceleration and deceleration, and the maximum position estimation error is only about 4.5°.

In the load step test, the DTP-IPMSM runs at 600 r/min, and the load command changes from no-load to 80% of the rated load, and then back to no-load. The test results are shown in Fig. 17 (a) - Fig. 17 (c), the largest speed estimation errors are 5 r/min. Again, dynamic errors only appear in the FA-LESO during loading and unloading, and the maximum position estimation error is approximately 3.2°.
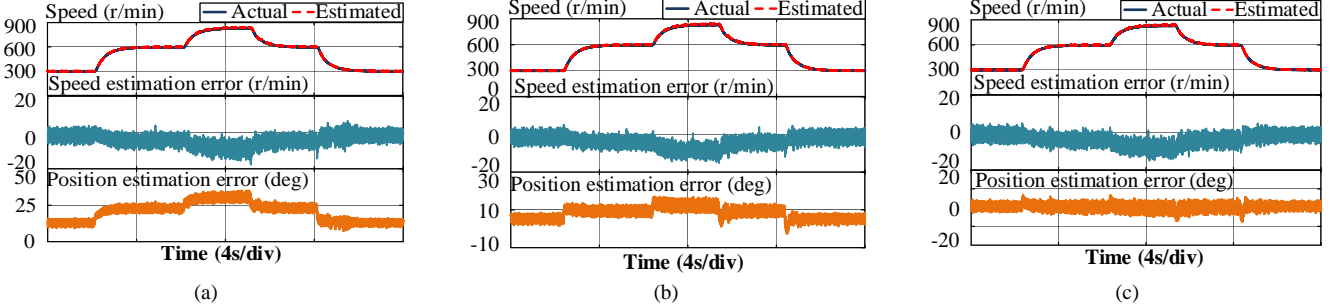
Fig. 16. Speed ramp test results at no-load and speed command changes as 300-600-840-600-300 r/min. (a) C-LESO. (b) GI-LESO. (c) FA-LESO.
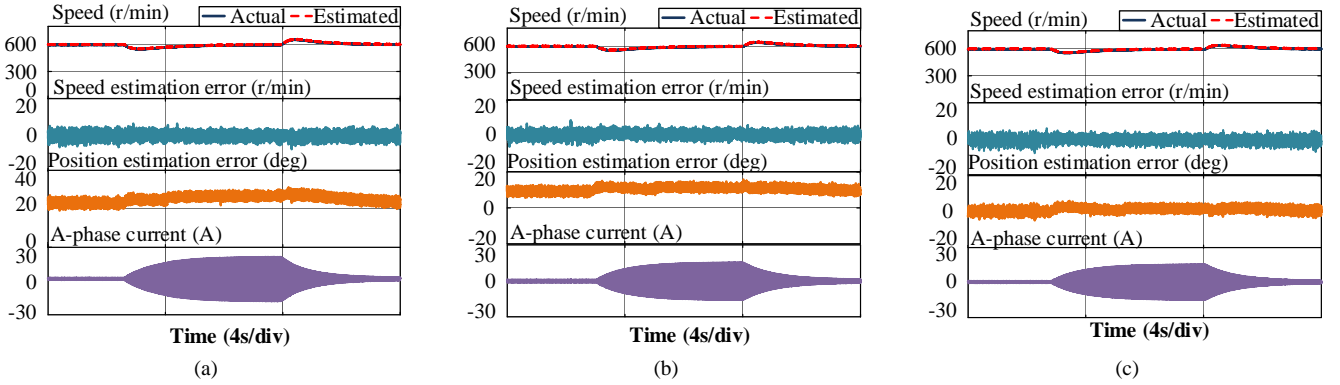
Fig. 17. Load step test results at 600 r/min (50 Hz). (a) C-LESO. (b) GI-LESO. (c) FA-LESO.

D. Robustness Test to Parameter Mismatches

Fig. 18 shows the test results of stator resistance R_s and q-axis inductance L_q mismatches at 300 r/min. The parameters change within the range of ± 0.5 p.u. According to (42) and (43), parameter mismatches do not affect position estimation error under no-load, therefore, the test under rated load is conducted. As can be seen in Fig. 18, the estimated equivalent BEMF of the α-axis hardly changes during the whole process. In addition, the position estimation error does not change during the overall period of stator resistance variation since the current control strategy $i_d^*=0$ is applied. However, there is a significant position estimation error during the overall period of q-axis inductance variation. This is consistent with (43) in Section III. (B). Therefore, the experimental results show that the influence of stator resistance variation can be negligible with the control strategy $i_d^*=0$; however, the inductance of q-axis inductance variation should be compensated to improve the accuracy of the position estimation, such as online tuning of the PMSM parameters, which is another popular research topic for scholars.
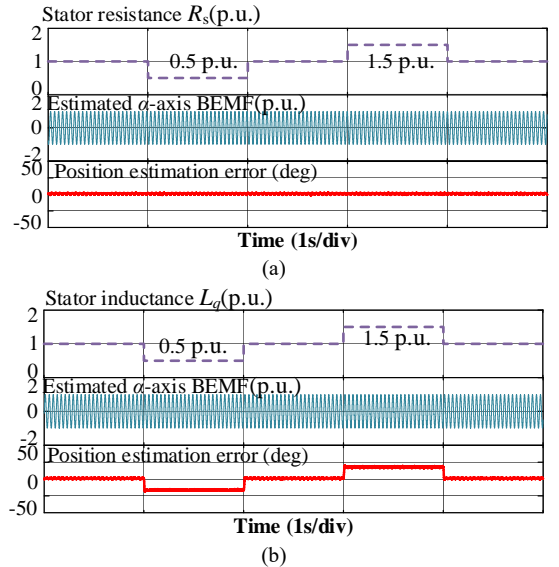
Fig. 18. Test results with parameter mismatches at 300 r/min (25 Hz) and rated load. (a) stator resistance mismatch. (b) q-axis inductance mismatch.

VI. CONCLUSION

This paper proposes a FA-LESO for the sensorless control of DTP-IPMSM, which is also suitable for general IPMSM. In the FA-LESO, the gains of the LESO are time-varying and a

design guideline is given for the gain function. The desired frequency characteristics of the observer can be obtained by a proper design of the gain function. The gains function is backstepping designed based on a pre-designed transfer function. The gains of the proposed observer are designed based on a linearized model. The comparative analysis with the C-LESO and the GI-LESO shows that the FA-LESO can eliminate the steady-state position error without any phase compensation. Meanwhile, it exhibits a better harmonics attenuation than the C-LESO and the GI-LESO. The steady-state and transient experimental results from the prototype DTP-PMSM demonstrate the feasibility and effectiveness of the proposed FA-LESO.

REFERENCES

[1] F. Barrero and M. J. Duran, "Recent advances in the design, modeling, and control of multiphase machines—Part I," *IEEE Trans. Ind. Electron.,* vol. 63, no. 1, pp. 449-458, 2016.

[2] Y. Hu, Z. Q. Zhu, and M. Odavic, "Torque capability enhancement of dual three-phase PMSM drive with fifth and seventh current harmonics injection," *IEEE Trans. Ind. Appl.,* vol. 53, no. 5, pp. 4526-4535, 2017.

[3] S. Jin, W. Zhao, J. Ji, and D. Xu, "Deadbeat fault-tolerant control scheme for dual three-phase PMSG with high-resistance connection fault," *IEEE Trans. Power Electron.,* vol. 38, no. 3, pp. 4015-4026, 2022.

[4] C. Wenping, B. C. Mecrow, G. J. Atkinson, J. W. Bennett *et al.*, "Overview of electric motor technologies used for more electric aircraft (MEA)," *IEEE Trans. Ind. Electron.,* vol. 59, no. 9, pp. 3523-3531, 2012.

[5] H. Yashan, Z. Zi-Qiang, and L. Kan, "Current control for dual three-phase permanent magnet synchronous motors accounting for current unbalance and harmonics," *IEEE J. Emerg. Sel. Topics Power Electron.,* vol. 2, no. 2, pp. 272-284, 2014.

[6] Y. Hu, Z. Q. Zhu, and M. Odavic, "Comparison of two-individual current control and vector space decomposition control for dual three-phase PMSM," *IEEE Trans. Ind. Appl.,* vol. 53, no. 5, pp. 4483-4492, 2017.

[7] Z. Zhu, A. Almarhoon, and P. Xu, "Improved rotor position estimation accuracy by rotating carrier signal injection utilizing zero-sequence carrier voltage for dual three-phase PMSM," *IEEE Trans. Ind. Electron.,* pp. 4454-4462, 2016.

[8] G. Wang, M. Valla, and J. Solsona, "Position sensorless permanent magnet synchronous machine drives—a review," *IEEE Trans. Ind. Electron.,* vol. 67, no. 7, pp. 5830-5842, 2020.

[9] B. Du, S. Wu, S. Han, and S. Cui, "Application of linear active disturbance rejection controller for sensorless control of internal permanent-magnet synchronous motor," *IEEE Trans. Ind. Electron.,* vol. 63, no. 5, pp. 3019-3027, 2016.

[10] L. Qu, W. Qiao, and L. Qu, "An enhanced linear active disturbance rejection rotor position sensorless control for permanent magnet synchronous motors," *IEEE Trans. Power Electron.,* vol. 35, no. 6, pp. 6175-6184, 2020.

[11] F. Jiang, S. Sun, A. Liu, Y. Xu *et al.*, "Robustness improvement of model-based sensorless spmsm drivers based on an adaptive extended state observer and an enhanced quadrature PLL," *IEEE Trans. Power Electron.,* vol. 36, no. 4, pp. 4802-4814, 2021.

[12] B. Yu, A. Shen, B. Chen, X. Luo *et al.*, "A compensation strategy of flux linkage observer in SPMSM sensorless drives based on linear extended state observer," *IEEE Trans. Energy Convers.,* 2021.

[13] Z. Xu, T. Zhang, Y. Bao, H. Zhang *et al.*, "A nonlinear extended state observer for rotor position and speed estimation for sensorless IPMSM drives," *IEEE Trans. Power Electron.,* vol. 35, no. 1, pp. 733-743, 2020.

[14] Z. Pu, R. Yuan, J. Yi, and X. Tan, "A class of adaptive extended state observers for nonlinear disturbed systems," *IEEE Trans. Ind. Electron.,* vol. 62, no. 9, pp. 5858-5869, 2015.

[15] J. Zhu, Q. Ge, and Q. Ge, "Extended state observer-based sensorless control for high-speed maglev application in single feeding mode and double-feeding mode," *IEEE Trans. Transp. Electrification.,* vol. 8, no. 1, pp. 1350-1361, 2022.

[16] C. J. V. Filho, D. Xiao, R. P. Vieira, and A. Emadi, "Observers for high-speed sensorless PMSM drives: Design methods, tuning challenges and future trends," *IEEE Access,* vol. 9, pp. 56397-56415, 2021.

[17] G. Zhang, G. Wang, D. Xu, and N. Zhao, "ADALINE-network-based PLL for position sensorless interior permanent magnet synchronous motor drives," *IEEE Trans. Power Electron.,* vol. 31, no. 2, pp. 1450-1460, 2016.

[18] Y. Zhang, Z. Yin, C. Bai, G. Wang *et al.*, "A rotor position and speed estimation method using an improved linear extended state observer for IPMSM sensorless drives," *IEEE Trans. Power Electron.,* vol. 36, no. 12, pp. 14062-14073, 2021.

[19] S. Chen, W. Ding, R. Hu, X. Wu *et al.*, "Sensorless control of PMSM drives using reduced order quasi resonant-based ESO and Newton–Raphson method-based PLL," *IEEE Trans. Power Electron.,* vol. 38, no. 1, pp. 229-244, 2022.

[20] Y. Zhao, Z. Zhang, W. Qiao, and L. Wu, "An extended flux model-based rotor position estimator for sensorless control of salient-pole permanent-magnet synchronous machines," *IEEE Trans. Power Electron.,* vol. 30, no. 8, pp. 4412-4422, 2015.

[21] X. Guo, W. Wu, and Z. Chen, "Multiple-complex coefficient-filter-based phase-locked loop and synchronization technique for three-phase grid-interfaced converters in distributed utility networks," *IEEE Trans. Ind. Electron.,* vol. 58, no. 4, pp. 1194-1204, 2010.

[22] F. Yang, F. Jiang, Z. Xu, L. Qiu *et al.*, "Complex coefficient active disturbance rejection controller for current harmonics suppression of IPMSM drives," *IEEE Trans. Power Electron.,* 2022.

[23] D. Xiao, S. Nalakath, Y. Sun, J. Wiseman *et al.*, "Complex-coefficient adaptive disturbance observer for position estimation of IPMSMs with robustness to DC errors," *IEEE Trans. Ind. Electron.,* vol. 67, no. 7, pp. 5924-5935, 2020.

[24] X. K. Xie, "Stable polynomials with complex coefficients," in *IEEE Conference on Decision & Control*, 1985.

[25] R. W. Hejny and R. D. Lorenz, "Evaluating the practical low-speed limits for back-emf tracking-based sensorless speed control using drive stiffness as a key metric," *IEEE Trans. Ind. Appl.,* vol. 47, no. 3, pp. 1337-1343, 2011.

[26] C. Wu, W. Xie, X. Wang, and D. Gerling, "A precise voltage distortion compensation strategy for voltage source inverters," *IEEE Trans. Ind. Electron.,* vol. 65, no. 1, pp. 59-66, 2018.

[27] C. Wu, Y. Zhao, and M. Sun, "Enhancing low-speed sensorless control of PMSM using phase voltage measurements and online multiple parameter identification," *IEEE Trans. Power Electron.,* vol. 35, no. 10, pp. 10700-10710, 2020.

[28] Y. Li, Y. Hu, and Z. Q. Zhu, "Current harmonics and unbalance suppression of dual three-phase PMSM based on adaptive linear neuron controller," *IEEE Trans. Energy Convers.,* pp. 1-11, 2023.

[29] T. Liu, Z. Q. Zhu, Z.-Y. Wu, D. Stone *et al.*, "A simple sensorless position error correction method for dual three-phase permanent magnet synchronous machines," *IEEE Trans. Energy Convers.,* vol. 36, no. 2, pp. 895-906, 2021.

[30] D. Xiao, S. Nalakath, Z. Xia, G. Fang *et al.*, "Computation-efficient position estimation algorithm for permanent magnet synchronous motor drives under distorted conditions," *IEEE J. Emerg. Sel. Topics Power Electron.,* vol. PP, no. 99, pp. 1-1, 2020.

[31] H. X. Nguyen, N. C. Tran, J. W. Park, and J. W. Jeon, "An adaptive linear-neuron-based third-order PLL to improve the accuracy of absolute magnetic encoders," *IEEE Trans. Ind. Electron.,* vol. 66, no. 6, pp. 4639-4649, 2019.

[32] Y. Hu, Y. Li, X. Ma, X. Li *et al.*, "Flux-weakening control of dual three-phase PMSM based on vector space decomposition control," *IEEE Trans. Power Electron.,* vol. 36, no. 7, pp. 8428-8438, 2021.